Open Access Full Text Article

ORIGINAL RESEARCH

# Enhanced Osteogenic Activity and Bone Repair Ability of PLGA/MBG Scaffolds Doped with ZIF-8 Nanoparticles Loaded with BMP-2

Rui Ma[1,]*, Yanwen Su[2,3,]*, Ruomu Cao[1], Kunzheng Wang[1], Pei Yang[1]

[1]Department of Bone and Joint Surgery, the Second Affiliated Hospital of Xi'an Jiaotong University, Xi'an, Shanxi, 710004, People's Republic of China; [2]State Key Laboratory for Manufacturing Systems Engineering, Xi'an Jiaotong University, Xi'an, 710049, People's Republic of China; [3]National Medical Products Administration (NMPA) Key Laboratory for Research and Evaluation of Additive Manufacturing Medical Devices, Xi'an Jiaotong University, Xi'an, 710049, People's Republic of China

*These authors contributed equally to this work

Correspondence: Kunzheng Wang; Pei Yang, Email wkzh1955@163.com; yangpei@xjtu.edu.cn

**Background:** Tissue engineering scaffolds are porous and can be loaded with growth factors to promote osteogenesis and bone repair, which can solve the problem of clinical bone defects. The direct loading of growth factors on scaffolds is hindered by the disadvantages of low loading capacities, and uncontrollable burst release. Zeolitic imidazolate framework-8 (ZIF-8) has osteoinductive activity and drug-loading potential and can be loaded with growth factors to achieve sustained release. In this study, we aimed to establish a sustained release system of composite scaffolds loaded with growth factors to achieve the goal of slow controlled release and effective bone repair.

**Methods:** ZIF-8 nanoparticles loaded with bone morphogenetic protein-2 (BMP-2) were incorporated into poly-(lactide-co-glycolide) /mesoporous bioactive glass (PLGA/MBG) porous scaffolds by a 3D-printing method. The surface morphology, chemical properties and BMP-2 release of the prepared scaffold were investigated. The osteoblast adhesion, proliferation, spreading, and osteogenic differentiation in vitro and the bone repair ability in vivo of the PLGA/MBG/ZIF-8/BMP-2 (PMZB) scaffold were evaluated, and compared with those of PLGA/MBG (PM) and PLGA/MBG/ZIF-8 (PMZ) scaffolds.

**Results:** The results showed that the PMZB scaffold exhibited a slow and continuous BMP-2 release pattern, enhanced osteoblast adhesion, proliferation, spreading and osteogenic differentiation in vitro, and promoted new bone formation and bone repair in vivo.

**Conclusion:** The PLGA/MBG/ZIF-8/BMP-2 porous scaffold could continuously and slowly release BMP-2, enhance osteogenic activity, and promote new bone formation and bone repair at bone defects. The PMZB scaffold can be used as a bone graft material to repair bone defect at non-weight-bearing sites.

**Keywords:** bone repair, controlled release, zeolitic imidazolate frameworks-8, mesoporous bioactive glass, scaffold

## Introduction

Bone defects caused by trauma, infection, tumors, and fracture nonunion are common in orthopedic clinics. Autologous or allogeneic bone grafts are usually used to restore the integrity of bone defects, but bone grafting is often restricted by limited tissue to harvest, reduced bioactivity, donor site morbidity, pathogen transmission risk and immune rejection.[1] Bone tissue engineering (BTE) scaffolds involve the use of biomaterials and growth factors that enhance cell differentiation, improve osteogenic activity and promote bone repair.[2,3]

To fabricate BTE scaffolds, poly (lactide-co-glycolide) (PLGA), polycaprolactone (PCL) and polylactic acid (PLA) have been widely used for bone tissue regeneration.[4,5] Among these polymer biomaterials, PLGA exhibits good biodegradability and biocompatibility,[6,7] and an injectable PLGA-based formulation has been approved by the Food and Drug Administration (FDA) of US as injectable PLGA-based formulations.[8] However, pure PLGA for bone regeneration is hampered by poor osteoconductivity, low hydrophilicity and suboptimal mechanical properties for use

in load-bearing applications,[6] and its acidic degradation byproducts can lead to a pH decrease in the vicinity of the implants.[9] 3D-printed composites composed of biodegradable polymers and bioceramics can benefit from the advantages of both phases and can be tailored to mimic the native bone structure.[2,3,10] 3D printed scaffolds play an essential role in supporting tissue reconstruction and remodeling.[10,11]

As a classic type of bioceramic with a composition of $CaO–SiO_2–P_2O_5$, mesoporous bioactive glasses (MBGs) possess favorable bioactivity and reasonable degradability.[12–15] MBG scaffolds have shown great potential for BTE and drug-delivery applications.[16,17] MBG incorporation improves the osteogenic ability of polymer-based composites.[9,18–21] Chen et al[21] prepared MBG-coated PLGA electrospun fibrous scaffolds, and found that the prepared MBG coated PLGA scaffold exhibited well bioactivity, promoted the attachment and proliferation of human mesenchymal stem cells (hMSCs). Wu et al[9] found MBG/PLGA films exhibited enhanced mechanical strength, in vitro degradation, apatite-formation ability, and pH stability in simulated body fluid (SBF), promoted human osteoblastic-like cell (HOB) differentiation, and possessed excellent drug-release properties compared to bioactive glass (BG)/PLGA. Shi et al[18] reported that nanosized MBG/PLGA-coated calcium silicate scaffolds improved physicochemical, biological, and drug-delivery properties as compared to conventional $CaSiO_3$ scaffolds. In another study, MBG/PLGA composite microspheres could be used as an antibiotic release system due to their combined advantages of sustained release and apatite-forming ability.[17,22] Thus, the MBG/PLGA composite scaffold was selected as the basic biomaterial for the bone scaffold in this study.

By using a tissue engineering method, growth factors can be loaded on biomaterials to prepare 3D-printed tissue engineered scaffolds, which have been used to repair bone defects.[23,24] One of the most widely used growth factor families in BTE is the bone morphogenetic protein (BMP) family, especially BMP-2.[3] BMP-2 has important roles during bone remodeling and homeostasis,[25] which regulates the osteogenic differentiation of hMSCs.[3] The FDA approved the use of recombinant BMP-2 during spinal fusion surgery, tibial shaft repair, and maxillary sinus reconstructive surgery.[25] However, directly loading growth factors in scaffolds has the disadvantages of low loading capacity and uncontrollable burst release. BMP-2 should be provided via a relatively sustained release system to achieve efficient bone regeneration.[26]

An ideal carrier of BMP-2 must achieve controlled sustained release, which promotes long-term BMP-2 activity within the specified environment without any ectopic growth. Metal-organic frameworks (MOFs), a new class of crystal materials with metal ions as the coordination center, have an extremely high specific surface area, high porosity, structural diversity, and unsaturated metal coordination bonds, which are conducive to modification with or grafting of other molecular substances.[27] Zeolitic imidazolate framework-8 (ZIF-8) is a type of MOF material with osteoinductive ability.[28] ZIF-8 possesses good stability, adjustable structure and function, and promising drug-delivery potential, and has gained increasing attention in tissue engineering applications.[29,30] Therefore, ZIF-8 was considered a suitable carrier of BMP-2 in the bone scaffolds in this study.

In this study, a novel scaffold system carrying growth factor was established to achieve a slow sustained release. ZIF-8 nanoparticles were first prepared, and BMP-2 was loaded into the ZIF-8 nanoparticles, then PLGA/MBG scaffolds doped with ZIF-8/BMP-2 were prepared using 3D-printing technology (Figure 1). However, whether this scaffold system could attain a controlled-release delivery and whether it could enhance osteogenic activity and bone repair ability were unknown. ZIF-8 nanoparticles were used as BMP-2 carrier to attain a controlled-release delivery profile and to avoid burst release of the growth factor. BMP-2 carrying ZIF8 nanoparticles were embedded in PLGA/MBG scaffolds to obtain a potential bone tissue substitute with bone repair ability. It was hypothesized that the PLGA/MBG/ZIF-8/BMP-2 scaffolds could slowly release BMP-2, promote osteoblast adhesion, proliferation, spreading, and osteogenic differentiation in vitro, stimulate new bone formation and promote bone repair in vivo.

# Materials and Methods
## Preparation of MBG Powders

MBG powders were synthesized as follows according to the previous report[31] with modifications. Typically, Pluronic P123 (2.0 g, 0.4 mmol; BASF, Frankfurt, Germany) was dissolved in HCl solution (75 mL, 120 mmol) at room temperature while being stirred for 60 min. Tetraethyl orthosilicate (4.4 g, 21 mmol) was added at 40 °C for 20 h,
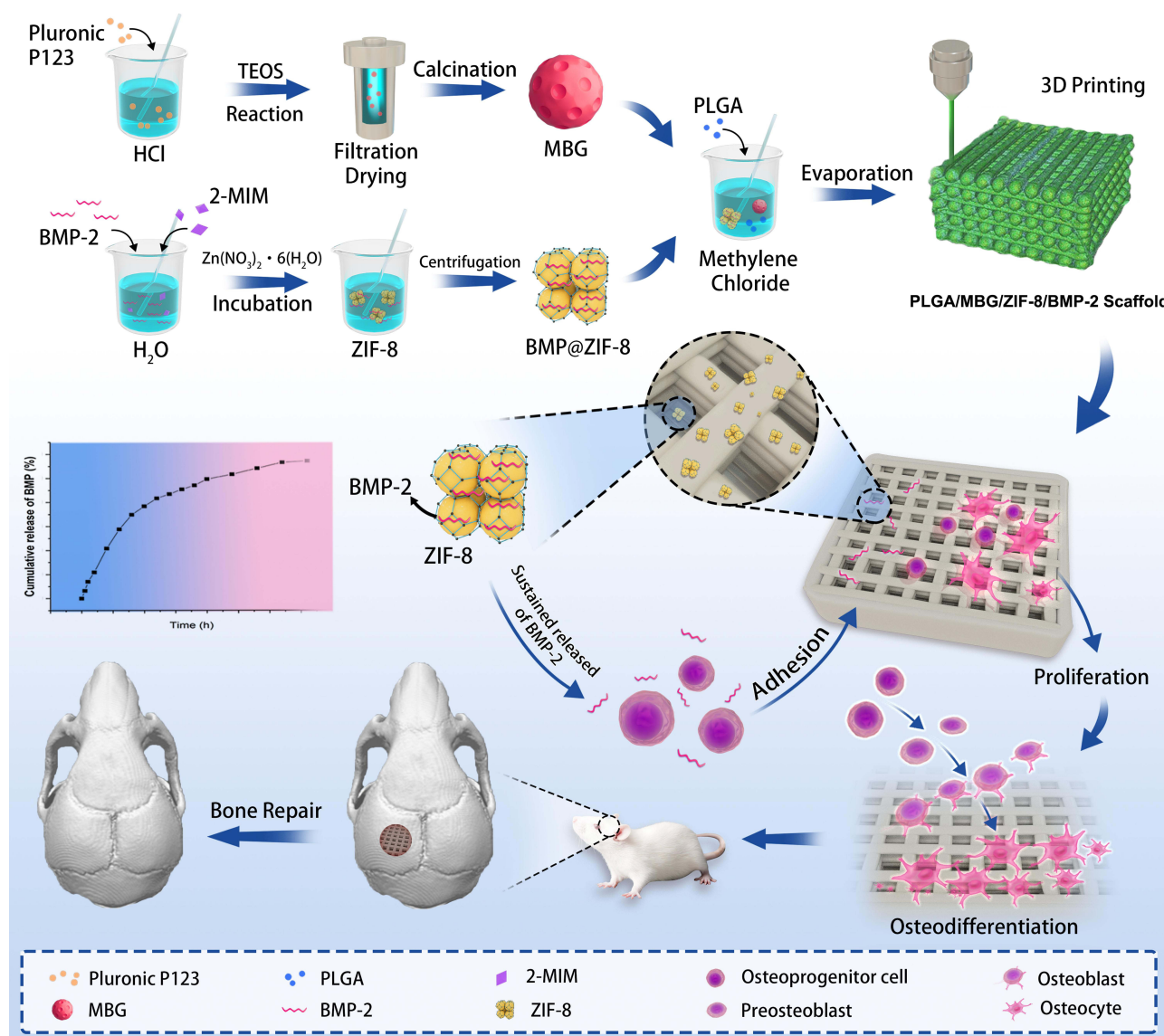
**Figure 1** Schematic diagram of the preparation and biological evaluation of the scaffold.
**Notes**: The MBG powders were synthesized by a sol-gel method. BMP@ZIF-8 nanoparticles were synthesized by a chemical synthesis method. The PLGA/MBG/ZIF-8/BMP-2 (PMZB) scaffold was fabricated by 3D-printing technology. The PMZB scaffolds could slowly release BMP-2, promote osteoblast adhesion, proliferation, spreading, and osteogenic differentiation in vitro, and stimulate new bone formation and promote bone repair in vivo.

and then transferred to an autoclave at 100 °C for 24 h. Afterwards, the mixture was cooled at room temperature, isolated by filtration, dried in air for 2 days, and calcined at 550 °C for 6 h. Finally, the remaining powders is the MBG powers.

## Preparation of BMP@ZIF-8 Nanoparticles

The synthesis method of BMP@ZIF-8 was as follows according to the previous report[32,33] with modifications. Briefly, 1 mg BMP-2 (polyclonal rabbit, Shanghai Yanhui Biotechnology Company, Shanghai, China) and 258 mg of 2-methy-limidazole (2-MIM) were first dissolved in 0.9 mL of deionized water. Then 13.38 mg of $Zn(NO_3)_2 \cdot 6(H_2O)$ in 0.1 mL of deionized water was added to the 2-MIM solution under vigorous stirring, and the solution was incubated for 10 min at 30 °C. The milk-white BMP@ZIF-8 nanoparticles were obtained by centrifugation at 13,000 rpm for 10 min and then washed twice with deionized water to remove the unreacted monomer. The ZIF-8 nanoparticles were prepared as the described procedure except without the addition of BMP-2.

## Fabrication of 3D-Printing Porous Scaffolds

First, PLGA (LA/GA=75/25, average molecular weight ≈ 15.5×10⁴, viscosity = 1.72 dL/g); Shandong Institute of Medical Instruments, Jinan, China) was dissolved in methylene chloride, and then MBG powders (PLGA: MBG mass ratio = 10: 1) were added. Then, the mixture was magnetically stirred for 8 h. BMP@ZIF-8 nanoparticles (PLGA: BMP@ZIF-8 mass ratio = 10: 1) were added to the solution. After further evaporation of the excess organic solvent in a fume cupboard, the homogeneous mixed compound was loaded into a 3D bioprinter (Envision TEC, Germany) for fabrication. Relevant parameters were set (pressure = 3.0 bar, speed = 10 mm s$^{-1}$, temperature = 37 °C, distance between strips = 800 mm, number of layers = 10), and the scaffold was shaped into a disc for (diameter = 10 mm, height = 3.2 mm) in vitro biological evaluations or a cylinder (5 × 5×15 mm) for in vivo animal studies. A nozzle with a diameter of 400 mm was selected. Finally, the prepared scaffolds were placed in a fume hood for another 48 h to fully volatilize the residual organic solvent.

The samples were prepared as the following three groups: (1) PLGA/MBG (PM): no addition of BMP@ZIF-8 nanoparticles; (2) PLGA/MBG/ZIF-8 (PMZ): no addition of BMP-2; and (3) PLGA/MBG/ZIF-8/BMP-2 (PMZB). All samples were sterilized with ethylene oxide.

## Characterization of MBG Powders and BMP@ZIF-8 Nanoparticles

The morphology of the MBG powders and BMP@ZIF-8 nanoparticles was observed by a transmission electron microscope (TEM, JEOL, JEM-100CX, Tokyo, Japan). The particle size distribution of the BMP@ZIF-8 nanoparticles was analyzed by Origin software (Electronic Arts Inc., USA). The N$_2$ adsorption/desorption isotherms and pore volume of the BMP@ZIF-8 nanoparticles were measured with a Micromeritics ASAP 2010 M instrument (USA).

## Characterization of the Scaffolds

After spraying with gold, the surface morphology of the scaffolds was observed by a scanning electron microscopy (SEM, SU8220, HITACHI, Tokyo, Japan). In addition, energy dispersive X-ray spectroscopy (EDS, X-Max, Horiba, Kyoto, Japan) was performed to observe the distribution of MBG and ZIF-8 in the scaffold. The compression moduli of the scaffolds (n = 5) were measured by a mechanical test machine (Instron 5567, Norwood, Massachusetts, USA).

## In vitro BMP-2 Release

Three scaffolds were soaked in 10 mL of phosphate-buffered saline (PBS) solution. The suspensions were placed into dialysis bags with a molecular weight cut off of 3000 Da, and subsequently placed in a beaker containing 100 mL of PBS with the same pH. The volume of the dissolution media was maintained at 100 mL while constantly stirring at 37 °C. At a predetermined time, 1 mL of PBS was submitted to high-performance liquid chromatography (HPLC) measurement using HPLC equipment (APS-8026PLUS, De Aupos scientific chromatographic technology, Henan, China) to calculate the released amount of BMP-2. The detection time points were 3, 6, 9, 18, 30, 38, 48, 56, 67, 78, 87, 96, 115, 135, 153, 174 hours.

## Cell Culture

MC3T3-E1 cells were used as experimental cells to evaluate the effect of materials on osteoblasts in vitro. MC3T3-E1 cells was purchased from the Typical Culture Preservation Commission Cell Bank, Chinese Academy of Sciences (Shanghai, China). The cell culture medium was Dulbecco's modified eagle medium (DMEM, HyClone, Thermo, USA) supplied with 10% fetal bovine serum (FBS, GibcoBRL, Grand Island, New York, USA), treptomycin sulfates (100 mg/mL, GibcoBRL, USA) and 1% penicillin (100 U/mL, GibcoBRL, USA) in a humidified cell incubator at 37 °C with 5% CO$_2$.

## Cell Adhesion and Proliferation

Prior to cell inoculation, the specimens were placed into cell culture plates with sterile tweezers with three specimens in each group. MC3T3-E1 cells that grew to 90% confluence were digested with 0.25% trypsin and counted with a cell counting plate. The density of the cell suspension was adjusted to 3×10⁴ cells/cm$^2$. The culture plates were cultured in the cell incubator. After 4, 12 and 24 h, the specimens were removed and washed several times with PBS. Then 50 μL of Cell

Counting Kit-8 (CCK-8) solution (Dojindo Molecular Technologies Inc., Kumamoto, Japan) was added to each well, and incubated for 3 h. 100 μL of the liquid was removed from each well and added to a 96-well plate. The optical density (OD) values at 450 nm and 620 nm were read using a microplate detector (Synergy HT, Biotek, Winooski, VT, USA). The effect of materials on cell proliferation was similarly assessed by the CCK-8 assay at 1, 3 and 7 days. The assay procedure was essentially the same as that in the cell adhesion assay, except that the cell density was $1 \times 10^4/cm^2$. The cells cultured on the tissue culture plate (TCP) served as the control group (CTL).

## Cell Morphology and Spreading

The cell spreading after staining the cytoskeleton with rhodamine-labeled phalloidin was observed by confocal laser scanning microscopy (CLSM). Cell samples were prepared according to the procedures in the cell adhesion assay. After 24 h, the material surface was washed three times with PBS and fixed with 4% paraformaldehyde for 20 min. The cells were permeabilized with 0.1% Triton X-100 (Sigma–Aldrich, USA) for 10 min. Then, 400 μL of rhodamine-phalloidin solution (5 U/mL, Biotium, Hayward, CA, USA) was added to stain for 30 min. Finally, the stained cytoskeleton was visualized using CLSM (TCS SP2, Leica, Heidelberg, Germany).

The morphology and spreading of cells on the material surfaces were observed by SEM at 24 h. Cell samples were prepared in the same way as those in the cell proliferation assay procedure. At 24 h, the cells were fixed with 2.5% glutaraldehyde for 20 min, washed three times with PBS, and dehydrated with an alcohol gradient from 30%, 50%, 70%, 90% to 100% (10 min for each gradient). The alcohol was then replaced with hexamethyldisilazane (HMDS, Sigma–Aldrich, USA) for 10 min. Finally, all samples were air-dried, gold sprayed, and observed by SEM (SEM, S-4800, Hitachi, Tokyo, Japan).

## Cell Osteo-Differentiation Culture

MC3T3-E1 cells were seeded onto the material surface at a density of $3 \times 10^4/cm^2$. After 24 h, the common medium was replaced with osteogenic induction medium. The osteogenic induction medium was prepared according to our previous study.[34] The osteogenic induction solution was changed every other day.

## Alkaline Phosphatase (ALP) Staining and Quantitative Analysis

After being cultured with osteogenic inductive medium for 7 and 14 days, the cells on the specimens were digested with 0.25% trypsin and cultured for 24 hours. ALP staining was performed with an ALP staining kit (Shanghai Renbao Ltd., Shanghai, China) according to the manufacturer instructions. ALP activity was determined through a colorimetric assay based on p-nitrophenyl phosphate according to previously published procedures.[34] The cells cultured on the TCP served as the control group (CTL).

## Alizarin Red (AR) Staining and Quantitative Analysis

After being cultured with osteogenic inductive medium for 21 and 28 days, the cells on the specimens were digested with 0.25% trypsin and cultured for 24 hours. Then the cells were fixed in 4% paraformaldehyde for 20 min, stained with 1% AR solution (pH=4.20; Sigma–Aldrich, USA) for 45 min, washed with deionized water for several times, and dried at 37 °C. Additionally, the cells cultured on the TCP served as the control group (CTL). Finally, images of all the stained samples were acquired using a digital scanner (Scanjet 2400, HP, Palo Alto, California, USA). For quantitative analysis, the orange staining on the samples was dissolved in 10% cetylpyridinium chloride (pH=7.0; Sigma–Aldrich) in 10 mM sodium phosphate (Sigma–Aldrich, USA), and the ODs were measured at 620 nm using a microplate detector[34] (Synergy HT, Biotek).

## Quantitative Analysis of Osteogenic Differentiation-Related Genes

The mRNA expression of mouse ALP, collagen type I (COL 1), osteoprotein (OPN), and osteocalcin (OCN) was analyzed via real-time polymerase chain reaction (RT-PCR). The transcription levels of genes were normalized to that of the β-actin housekeeping gene (the primers are shown in Table 1). Total RNA was collected from the cells on the materials using TRIzol reagent (Ambion, Grand Island, New York, USA) according to the manufacturer instructions.

**Table 1** Primers Used in the Real-Time PCR Tests

| Target Genes | Primer Sequences (5' → 3') | |
|---|---|---|
| ALP | F: GGGCATTGTGACTACCACTCG | R: CCTCTGGTGGCATCTCGTTAT |
| COL1 | F: AACAGTCGCTTCACCTACAGC | R: GGTCTTGGTGGTTTTGTATTCG |
| OPN | F: CTTTCACTCCAATCGTCCCTAC | R: CCTTAGACTCACCGCTCTTCAT |
| OCN | F: GGACCATCTTTCTGCTCACTCTG | R: TTCACTACCTTATTGCCCTCCTG |
| β-actin | F: GAGACCTTCAACACCCCAGC | R: ATGTCACGCACGATTTCCC |

**Abbreviations**: ALP, alkaline phosphatase; COL1, collagen type I; OPN, osteoprotein; OCN, osteocalcin; F, forward, R, reverse.

Reverse transcription was performed by a Revert-Aid First Strand cDNA Synthesis Kit (Fermentas, Thermo Scientific Molecular Biology, Pittsburgh, Pennsylvania, USA) according the manufacturer's protocol. Quantitative RT-PCR was performed using the SYBR premix EX Taq II PCR kit (TaKaRa Biotechnology Co., Dalian, China).

## Animal Surgery

All animal experiments and the related experimental protocols used in the present study were approved by the Second Affiliated Hospital of Xi'an Jiaotong University and were carried out in accordance with the UK Animals (Scientific Procedures) Act (1986). A total of 12 SD rats (male, 180–220 g) were used for the calvaria defect experiment. They were divided into four groups: blank control, PM, PMZ and PMZB. There were 6 samples (3 rats) in each group. The rats were intraperitoneally injected with 10% chloral hydrate (4 mg/kg). After successful anesthesia, the rats were placed in a supine position on the operating table and fixed. The rats were routinely disinfected with iodophor. The skin was incised along the long axis of the parietal bone, and the periosteum was peeled off to expose the parietal bone. A trephine was placed in the center of the bilateral parietal bone, and a bone defect with an outer diameter of 5 mm was drilled out by a trephine. After drilling through the outer plate and barrier, the inner plate was drilled slowly and with care. Then the specimens were implanted into the bone defects. The periosteum was sutured as intact as possible, the incision was sutured tightly layer by layer, and the wound was sterilized with iodophor. After the operation was completed, each rat was injected with 10,000 U of penicillin intramusitoneally per day for 3 days. The X-ray radiographs were taken at 4 w and 12 w after implantation using a dual-energy X-ray analyzer (iNSight VET DXA, Osteosys, Korea).

## Micro-CT Analysis

At 12 weeks, all rats were sacrificed, the parietal bones were taken out. Then, the specimens were soaked in 75% ethanol for 1 week, and dehydrated with 80%, 95%, and 100% ethanol for 2 days for each gradient. The specimens were scanned by a micro-CT instrument (Venus 001, Pingseng Healthcare, China) and reconstructed at 21 μm (resolution) with reconstruction and analysis software (Avatar 3).

## Histological Evaluation

The process of preparation of histological section was the same as our previous study.[35] The sections of each implant were stained with Masson's staining. The histological morphology of the implant/bone interfaces was observed by a light microscope (Leica Microsystems AG, Wetzlar, Germany). The new bone tissue areas of Masson's staining were measured by histomorphology using Image J software.

## Statistical Analysis

All statistical analyses were performed using Statistical Product and Service Solutions (SPSS) software (IBM SPSS Statistics 19). All in vitro experiments were conducted in triplicate and repeated three times. Statistical significance was calculated using two-way analysis of variance and least significant difference post hoc tests. When p value < 0.05, the difference was considered statistically significant.

# Results

[Figure 2](#) shows the characterization analysis of the prepared ZIF-8 nanoparticles. The synthesized ZIF-8 was octahedral ([Figure 2A](#)) with a size between 70–200 nm, and the particle size distribution showed that the maximum size was 127.7 ± 28.59 nm ([Figure 2B](#)). As shown in the pore adsorption curve ([Figure 2C](#)), the isotherm increased rapidly at a relatively low pressure, and the adsorption appeared to reach saturated saturation after a certain pressure, indicating that ZIF-8 nanoparticles exhibited a high specific surface area and many micropores on their surfaces. [Figure 2D](#) shows that the size of the micropores on the ZIF-8 nanoparticle surface was approximately 1 nm. These micropores facilitated the encapsulation and loading of BMP-2 molecules.

As shown in [Figure 3A](#), the synthesized MBG powder had a rod-like or spherical shape with a size of approximately 100–300 nm. The BMP-2 release curve ([Figure 3B](#)) showed a slow BMP-2 release pattern. BMP-2 release was slightly rapid and the released content of BMP-2 reached approximately 40% within 72 h; then, the release slowed down gradually. At 174 h, the release content reached approximately 57%, and the release was supposed to continue. SEM images of the scaffold materials showed that the PM scaffold surface had a typical three-dimensional porous structure with square pores, while the PMZ and PMZB scaffold surfaces exhibited fine reticular structures that covered the 3D porous structure, which was exhibited more obviously by the PMZB scaffold surface ([Figure 3C](#)). The EDS spectra showed that the main elements on the PMZB scaffold surface were C, Ca, P, O and Mg ([Figure 3D](#)). The compressive strength of the PMZ and PMZB scaffolds was 2.89 ± 0.22 MPa and 2.90 ± 0.30 MPa, respectively, which was higher than that of the PM scaffolds (2.32 ± 0.30 MPa) ($p < 0.05$; [Figure 3E](#)), and was within the range of human cancellous bones (2–12MPa).[36]

Cell adhesion and proliferation on the material surface were quantitatively analyzed by the CCK-8 assay, and the OD values represented the numbers of cells. As shown in [Figure 4](#), at each time point in the cell adhesion test, no significant difference was found in the cell numbers among the three groups in cell adhesion test ($p > 0.05$). At 3 and 7 days, the cell
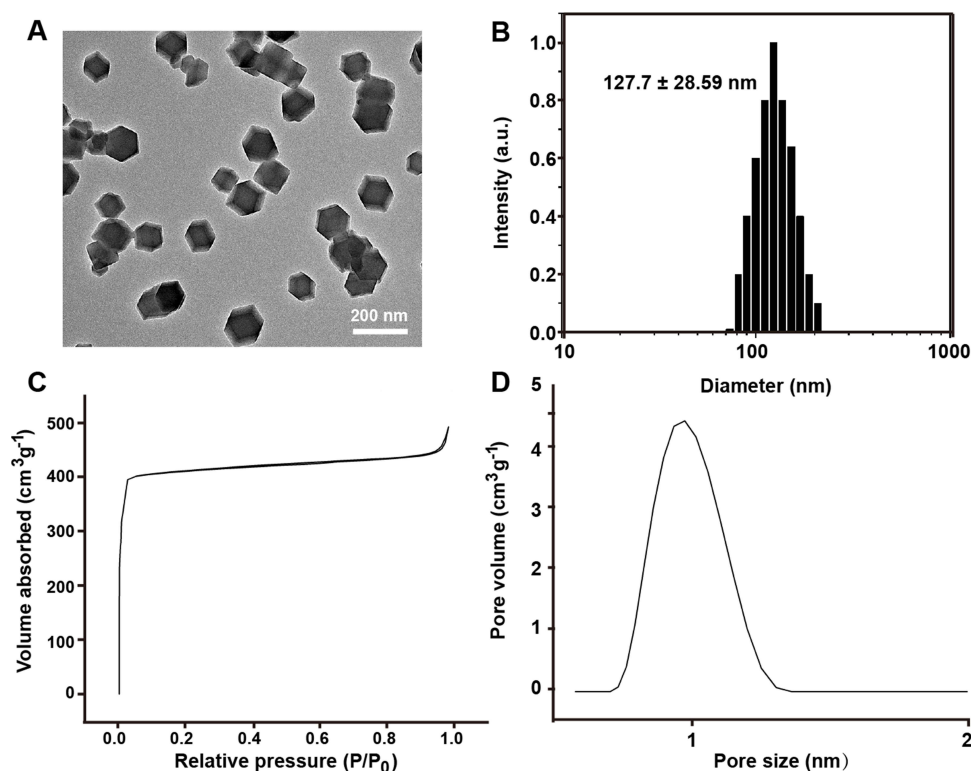


**Figure 2** Characterization of BMP-2@ZIF-8 nanoparticles.
**Notes**: (**A**) TEM image; (**B**) particle size distribution; (**C**) pore type analysis; (**D**) pore size analysis.
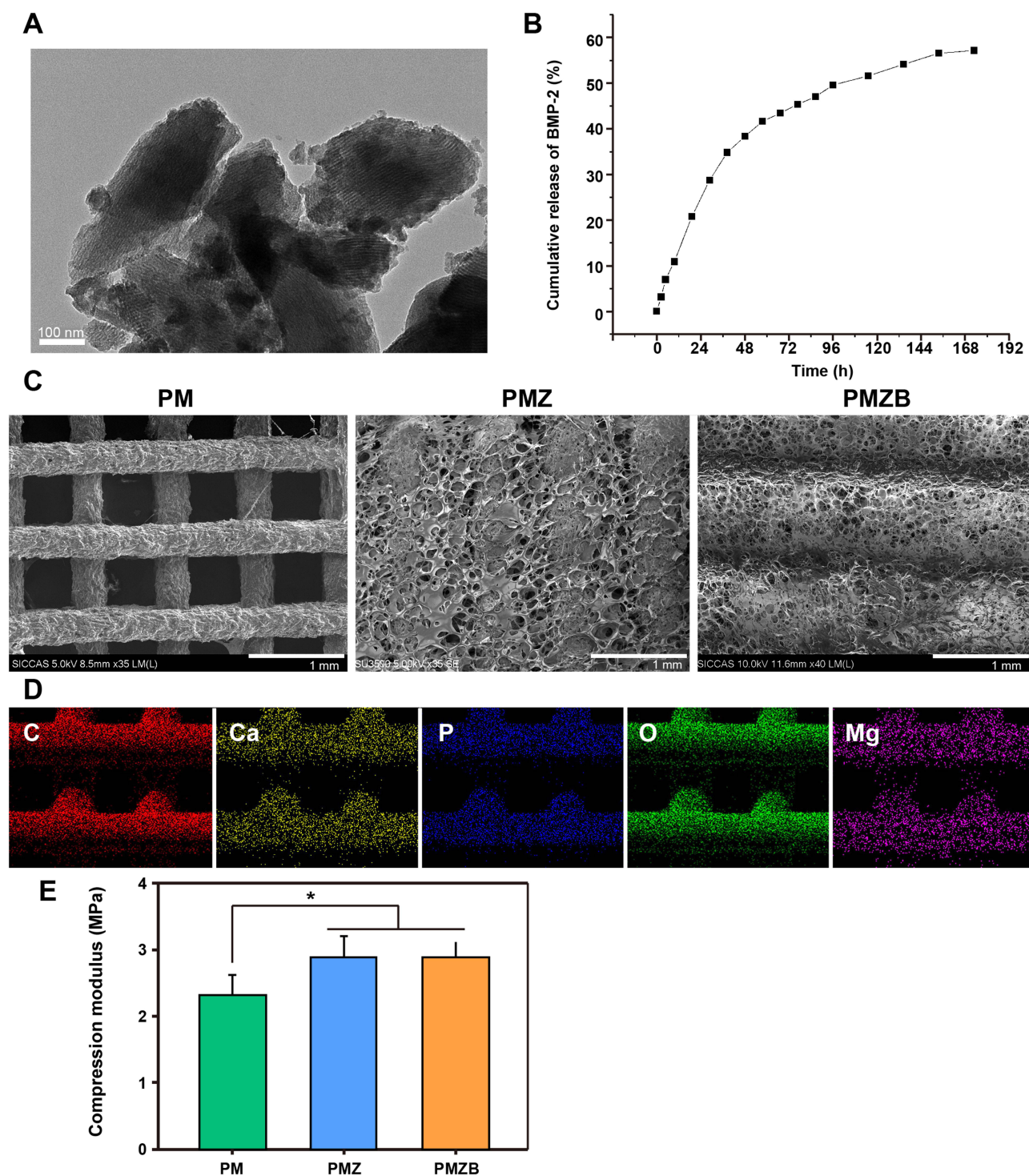
**Figure 3** Material characterization of the MBG powders and PLGA/MBG/ZIF-8/BMP-2 scaffold.
**Notes**: (**A**) TEM image of MBG powders; (**B**) BMP-2 release pattern of the PMZB scaffold; (**C**) SEM images of the PM. PMZ and PMZB scaffolds; (**D**) EDS images of the PMZB scaffold; (**E**) compression moduli of the scaffolds. *Significant differences between each pair of groups.
**Abbreviations**: BMP-2, bone morphogenetic protein-2; PM, PLGA/MBG; PMZ, PLGA/MBG/ZIF-8; PMZB, PLGA/MBG/ZIF-8/BMP-2.

numbers on the material surface were significantly different between each pair of groups ($p < 0.05$). The decreasing order of the cell numbers on the material surfaces in each group was PMZB group > PMZ group > PM group > control group.

The cytoskeleton stained with phalloidin was visualized by CLSM to assess the spreading of cells on the material surfaces. The cytoskeleton staining results are shown in Figure 4C. The cells on the PMZB scaffold surface spread
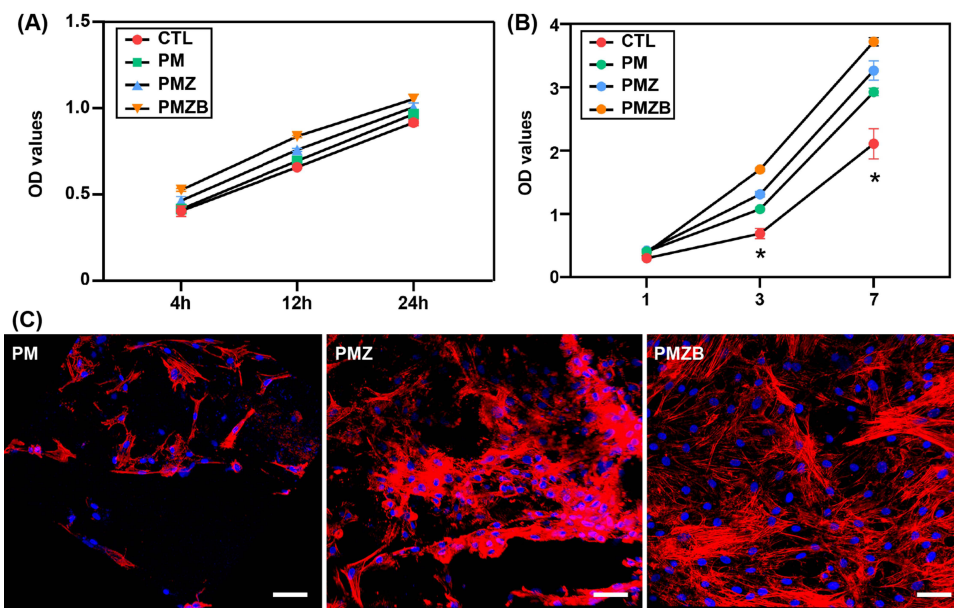
**Figure 4** Cell adhesion and proliferation assessed by the CCK-8 assay, and cell spreading observed by CLSM.
**Notes**: (**A**) Cell adhesion of different groups after 4, 12 and 24 hours; (**B**) cell proliferation of different groups after 1, 3 and 7 days; (**C**) cytoskeleton stained with phalloidin after 24 hours. The scale bar is 50 μm. The cells cultured on the TCP served as the CTL group. *Significant differences between each pair of groups.
**Abbreviations**: CTL, control; PM, PLGA/MBG; PMZ, PLGA/MBG/ZIF-8; PMZB, PLGA/MBG/ZIF-8/BMP-2.

efficiently, with well-formed cytoskeletal organization and a large number of interconnected actin microfilaments. The number of cells on the PMZ scaffold surface seemed higher than that on the PM scaffold surface, and the spreading efficiency of the cytoskeleton of the cells on the PMZ scaffold surface was better than that of cells on the PM scaffold surface. The cells on the PM scaffold surface were dispersed and had few actin filaments.

The cell morphology on the material surface were observed by SEM, as shown in Figure 5. A large number of cells on the PMZB scaffold surface were flat and well-spread, and were growing in the pores and on the columns between the pores, and abundant pseudopodia and filaments were extended between the cells to anchor them to the material surface and to connect with each other. The cells on the PMZ scaffold surface were not intimately connected, with few pseudopodia and filaments. The cells on the PM scaffold surface were atrophied and sparsely distributed.
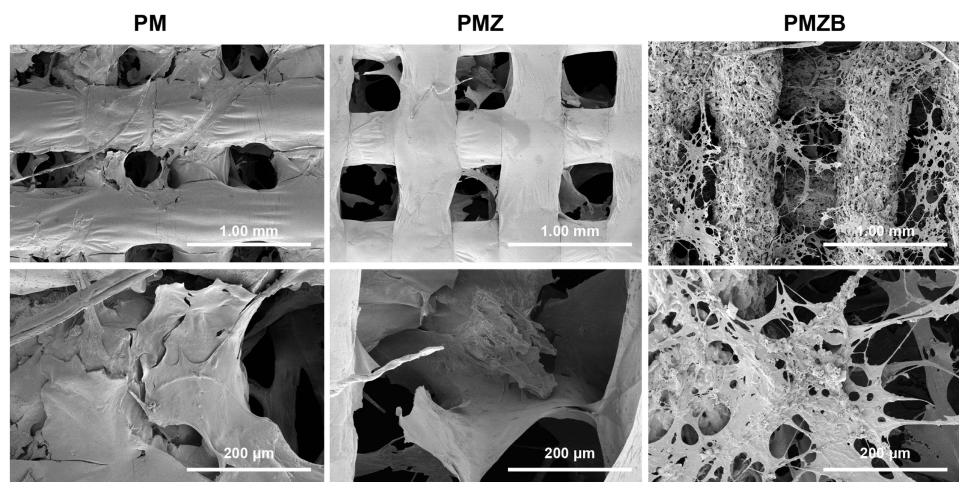


**Figure 5** Cell spreading and morphology observed by SEM after 24 hours.
**Notes**: The low-magnification images are shown in the upper row, and the scale bar is 1 mm. The high-magnification images are shown in the lower row, and the scale bar is 200 μm.
**Abbreviations**: PM, PLGA/MBG; PMZ, PLGA/MBG/ZIF-8; PMZB, PLGA/MBG/ZIF-8/BMP-2.

Figure 6 shows the ALP staining and ALP activity quantitative analysis results. According to the qualitative ALP staining results (Figure 6A) at 7 and 14 days, the intensity of ALP staining on the PMZB scaffold surface was significantly stronger than that on the other scaffold surfaces, and the ALP staining intensities on the PMZ and PM scaffold surfaces were stronger than that on the control group. At each time point, the decreasing order of ALP activity was PMZB group > PMZ group > PM group > control group, with statistically significant differences between each pair of groups ($p < 0.05$).

AR staining and quantitative analysis were used to evaluate the calcium nodule formation, and the results are shown in Figure 7. According to the AR staining results (Figure 7A), the AR staining intensities on the PMZB and PMZ scaffold surfaces were significantly stronger than those on the other two scaffold surfaces, and the AR staining intensity on the PM scaffold surface was significantly stronger than that on the control group. According to the quantitative AR staining results (Figure 7B and C), the number of calcium nodules on the material surfaces followed the decreasing order of PMZB group > PMZ group > PM group > control group at 21 and 28 days, and the differences between each pair of groups were statistically significant ($p < 0.05$).

Figure 8 shows the real-time quantitative PCR results of the osteogenic differentiation-related genes of MC3T3-E1 cells on the material surfaces. At 7, 14 and 21 days, the decreasing order of ALP expression was PMZB group > PMZ group > PM group > control group, and the differences between each pair of groups were statistically significant ($p < 0.05$). The expression of COL1 in cells on the PMZB group was significantly higher than that in the other three groups at 7 and 21 days ($p < 0.05$). At 14 days, the PMZ and PM groups exhibited significantly higher COL1 expression than the control group ($p < 0.05$). The expression of OPN in cells in the PMZB group was significantly higher than that in the other three groups at 7, 14 and 21 days ($p < 0.05$). At 7 and 21 days, the PMZ and PM groups had significantly higher OPN expression than the control group ($p < 0.05$). The OCN expression of cells followed the decreasing order of PMZB
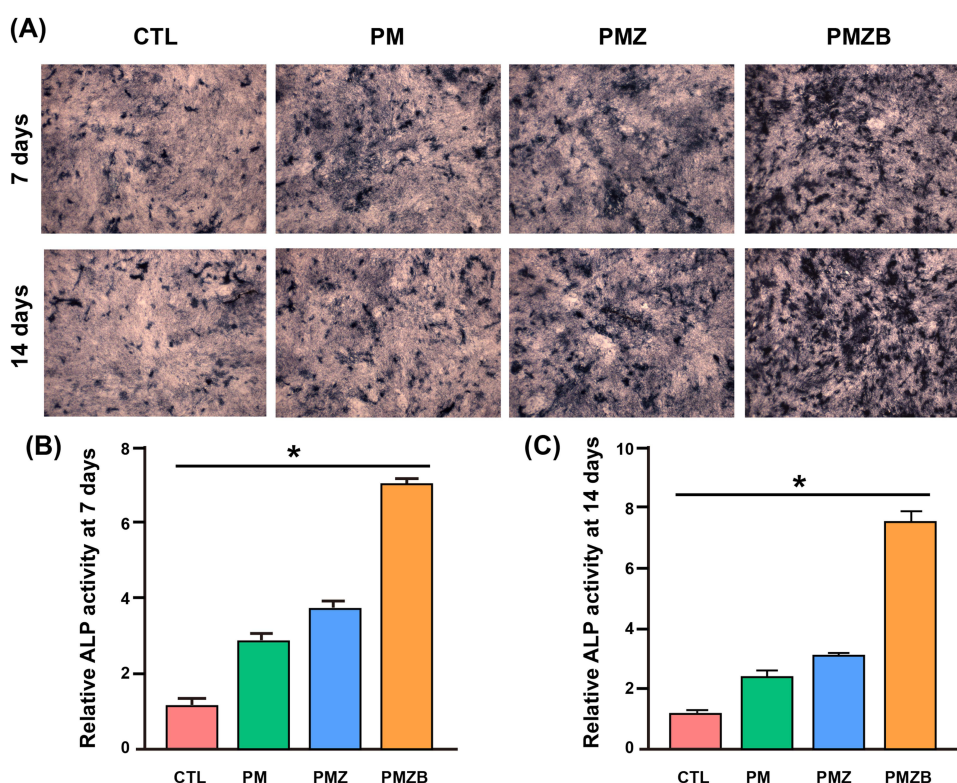


**Figure 6** ALP staining (**A**) and ALP activity measured by a quantitative colorimetric assay (**B** and **C**) after incubation for 7, 10 and 14 days.
**Notes**: The cells cultured on the TCP served as the CTL group. *Significant differences between each pair of groups.
**Abbreviations**: CTL, control; PM, PLGA/MBG; PMZ, PLGA/MBG/ZIF-8; PMZB, PLGA/MBG/ZIF-8/BMP-2; ALP, alkaline phosphatase.
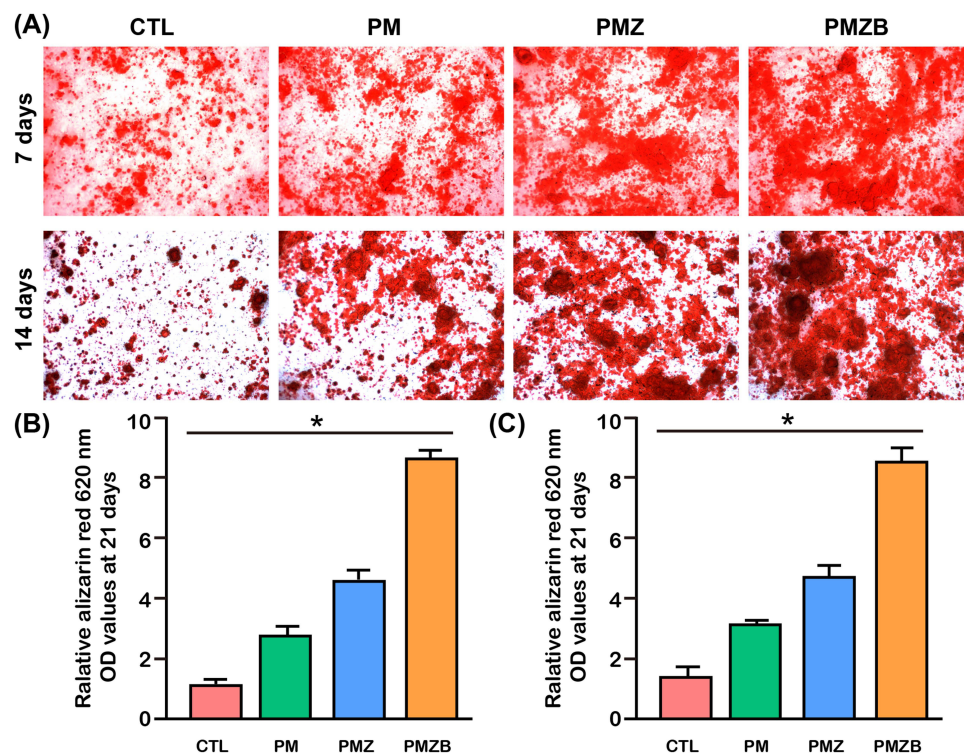
**Figure 7** Alizarin red (AR) staining and quantitative analysis of MC3T3-E1 cells on the material surfaces at 21 and 28 days.
**Notes**: (**A**) AR staining of different groups; (**B**) quantitative analysis of AR staining at 21 days; (**C**) quantitative analysis of AR staining at 28 days. The cells cultured on the TCP served as the CTL group. *Significant differences between each pair of groups.
**Abbreviations**: CTL, control; PM, PLGA/MBG; PMZ, PLGA/MBG/ZIF8; PMZB, PLGA/MBG-ZIF8/BMP2; OD, optical density.

group > PMZ group > PM group > control group at 7, 14 and 21 days, with significant differences between each pair of groups (p < 0.05).

Figure 9 shows the X-ray images taken at 4 and 12 weeks after material implantation at the bone defects. With increasing the implantation time, the transparent areas of the bone defects in the PMZB and PMZ groups gradually decreased and the densities gradually increased, which proved that new bone gradually formed to repair the bone defects. However, the changes in the PM group and the blank control group were not obvious.

Figure 10 shows the micro–CT images and quantitative analysis results at 12 weeks after material implantation. New bone formation around the bone defects was not obvious in the blank control group and the PM group. In the PMZ group, the new bone around the bone defect gradually grew to the center of the bone defect. Abundant new bone formed and covered most of the area of the bone defect in the PMZB group. Quantitative analysis showed that the bone volume (BV)/total volume (TV) and bone mineral density (BMD) in the PMZB group were significantly higher than those in the PM group, PMZ group and blank control group (p < 0.05). The BV/TV and BMD in the PMZ group were significantly higher than those in the blank control group (p < 0.05). The BV/TV in the PM group was significantly higher than that in the blank control group (p < 0.05).

Figure 11 shows the Masson's trichome staining results at 12 weeks after material implantation. New bone formation was the most obvious in the PMZB group, a small amount of new bone formation was observed in the PMZ group, and no obvious new bone formation was observed in the PM group and the blank control group (Figure 11A). In addition, there was no apparent material residue in the PM, PMZ and PMZB groups. The new bone tissue area of the PMZB group was 16.3 ± 2.1%, which was obvious higher than those of the PMZ (1.3 ± 0.6%), PM (0.2 ± 0.1%) and blank groups (0%) (p < 0.05; Figure 11B).
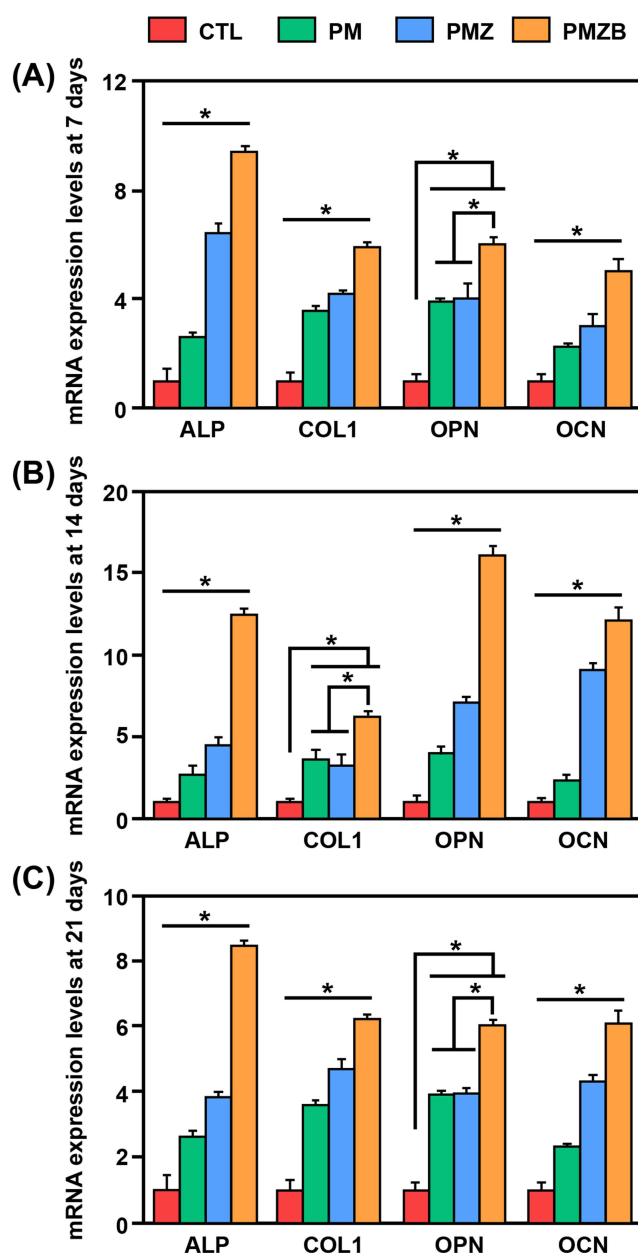
**Figure 8** Real-time quantitative PCR results of the osteogenic differentiation genes of MC3T3-E1 cells on the material surfaces at 7, 14 and 21 days.
**Notes**: (**A**) Day 7; (**B**) day 14; (**C**) day 21. The cells cultured on the TCP served as the CTL group. *Significant differences between different groups.
**Abbreviations**: CTL, control; PM, PLGA/MBG; PMZ, PLGA/MBG/ZIF-8; PMZB, PLGA/MBG/ZIF-8/BMP-2; ALP, alkaline phosphatase; COL1, collagen type I; OPN, osteoprotein; OCN, osteocalcin.

# Discussion

Using 3D-printing technology, it is feasible to precisely and rapidly fabricate 3D interconnected porous tissue engineering scaffolds.[7] Various nanomaterials have been applied in bone tissue engineering and medical application.[37–39] Tissue engineering scaffolds with nanomaterials can be loaded with growth factors to enhance their osteogenic activity and bone repair ability. Porous scaffold materials can gradually degrade and slowly release growth factors to promote new bone formation and bone regeneration, and then promote bone repair at bone defects. However, no single material or strategy has yet achieved the required spatiotemporal release due to the disadvantages of low growth factor loading capacity, low stability, short release and uncontrolled release.[40]
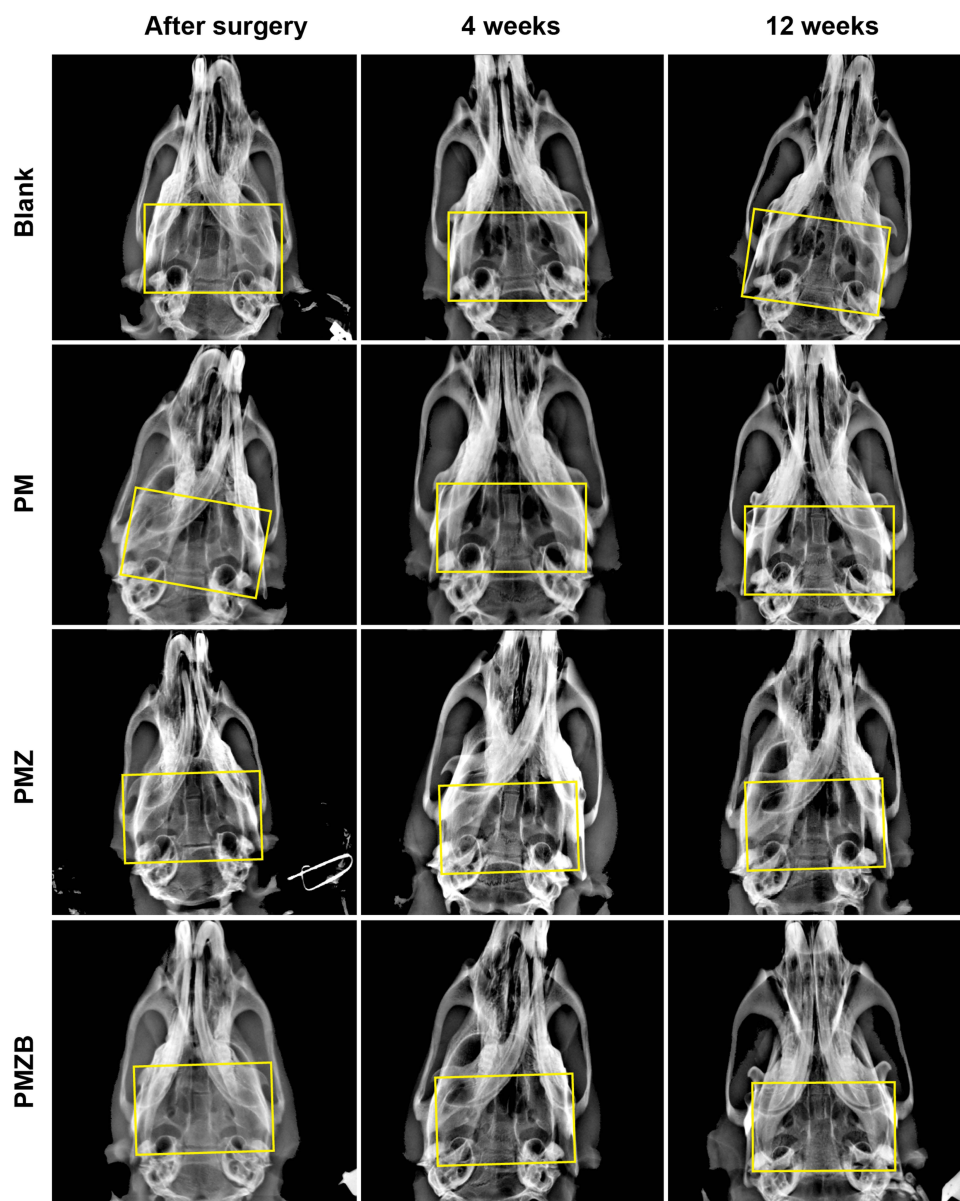
|  | After surgery | 4 weeks | 12 weeks |
|---|---|---|---|



**Figure 9** X-ray images taken at 4 and 12 weeks after material implantation at the bone defects.
**Abbreviations**: PM, PLGA/MBG; PMZ, PLGA/MBG/ZIF-8; PMZB, PLGA/MBG/ZIF-8/BMP-2.

BMP-2 is an important osteoinductive growth factor that is approved by the US FDA for clinical use to induce bone formation via the enhancement of osteoblast progenitor cell recruitment and angiogenesis, and the stimulation of the MSC osteogenic differentiation.[41,42] To achieve sustained controlled BMP-2 release, a preferable candidate for BMP-2 delivery is highly desired. ZIF-8 has been extensively studied in the medical field due to its high porosity, good structural tunability, adjustable surface functionality and appropriate biodegradability.[29] The high porosity of ZIF-8 nanoparticles allows it to encapsulate a large amount of growth factors[30] and control the release of these loaded growth factors.[43] In this study, ZIF-8 nanoparticles loaded with BMP-2 were first prepared, and then the BMP-2@ ZIF-8 nanoparticles were incorporated into a PLGA/MBG composite to prepare a sustained-release scaffold system by a 3D-printing method. The ZIF-8 particles were nanoscale and porous with a high specific surface area, which was beneficial for BMP-2 loading. The PLGA/MBG composite served as a matrix material to dope with the BMP-2@ZIF-8 nanoparticles and to contribute mechanical support. Both the PLGA/MBG composite and the ZIF-8 nanoparticles exhibited appropriate biodegradability, which could create favorable conditions for the slow release of BMP-2.
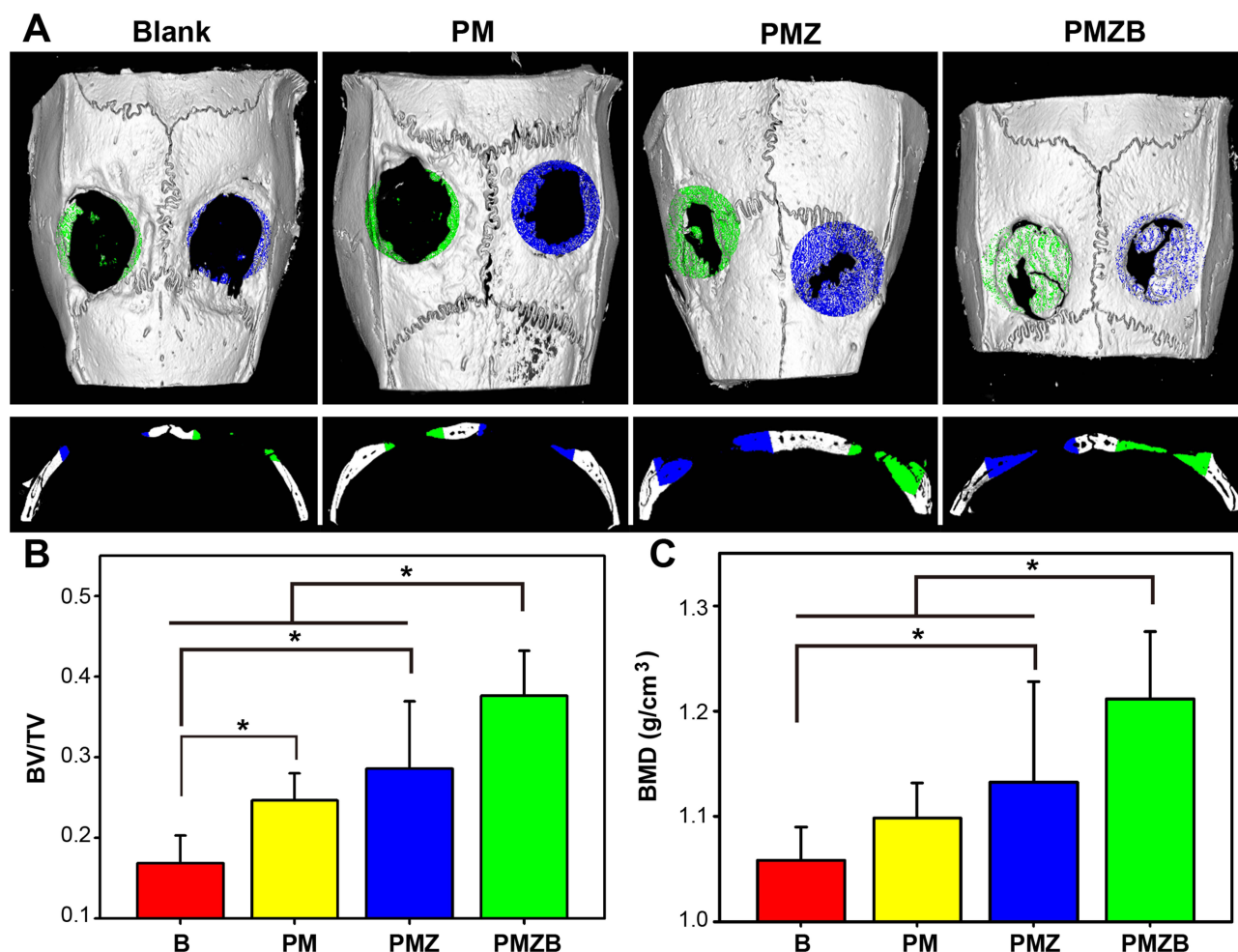
**Figure 10** Micro–CT images and quantitative analysis results at 12 weeks after material implantation.
**Notes**: (**A**) Micro-CT reconstruction; (**B**) quantitative analysis of BV/TV; (**C**) quantitative analysis of BMD. *Significant differences between different groups.
**Abbreviations**: PM, PLGA/MBG; PMZ, PLGA/MBG/ZIF-8; PMZB, PLGA/MBG/ZIF-8/BMP-2; BV, bone volume; TV, total volume; BMD, bone mineral density; B, blank.

    In this study, approximately 40% of the total BMP-2 was released about 40% within 72 h; only 57% of the total BMP-2 was released at 174 h (7.25 days), and the residual BMP-2 was continuously released over a long time. Therefore, the PMZB scaffold achieved sustained release without burst release. Some researchers used MBG to load gentamicin (GS) and found that GS release from the MBG was very fast with approximately 60% in the first 24 h (burst release), and more than 80% was released in two days (without sustained release).[17] When they used PLGA/MBG to load GS, they found that MBG/PLGA composite microspheres showed an initial release of approximately 33% in the first day, and 48% in 2 days,[17] which is a faster release than that of the PMZB scaffold in this study. In another study, copper (Cu)-loaded ZIF-8 nanoparticles and PLGA were combined to fabricate porous PLGA/ZIF8-Cu scaffolds using 3D printing technology, and the Cu ions were slowly and continuously released from PLGA/ZIF8-Cu scaffolds over 25 days.[44] Based on previous literature,[29] it could be assumed that the PMZB scaffold exhibited third-level sustained drug release:[29] (1) BMP-2 was directly released from the pore surface; (2) BMP-2 was released in a delayed manner after the disappearance of the coordination between BMP-2 and the metal coordination centre; and (3) BMP-2 was completely released, accompanied by the degradation of ZIF-8 and PLGA/MBG. These results indicated that the ZIF-8 nanoparticles in the PLGA/MBG scaffold were excellent sustained-release carriers.

    The interaction between a biomaterial and osteoblasts is an important indicator of the biocompatibility and bone bioactivity of the biomaterial. Favorable tissue engineering scaffolds can elicit physical and chemical signals to support cell adhesion, spreading, proliferation and differentiation. Osteoblast initial adhesion and spreading are very important
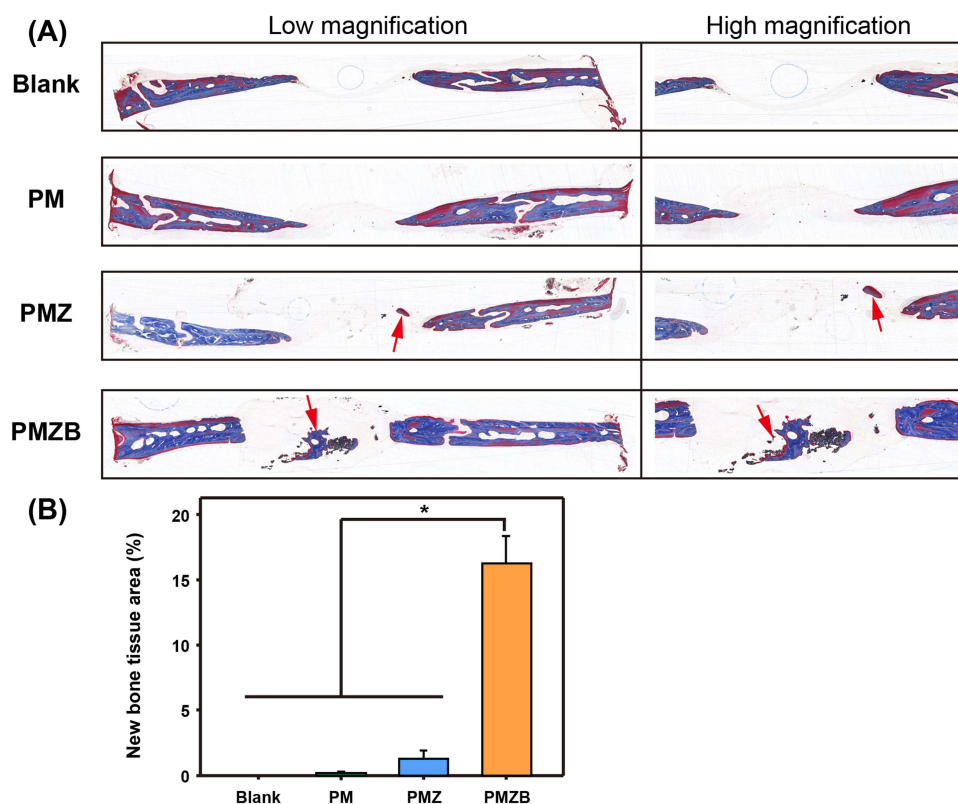
(A)



(B)



**Figure 11** Masson's trichome staining results at 12 weeks after material implantation.
**Notes**: (**A**) Representative photos; (**B**) quantitative analysis. The red arrows indicate newly formed bone tissues. *Significant differences between different groups.
**Abbreviations**: PM, PLGA/MBG; PMZ, PLGA/MBG/ZIF-8; PMZB, PLGA/MBG/ZIF-8/BMP-2.

for subsequent cell proliferation and differentiation.[45,46] In this study, it was found that spreading and proliferation of MC3T3-E1 cells on the material surface in the PMZB group was significantly promoted, compared to those in the PMZ, PM and CTL groups. The improvement in proliferation was attributed to the increased surface hydrophilicity (compared to that in the CTL group), the degradation products of MBG (compared to those in the CTL group), the addition of ZIF-8 (compared to that in the CTL and PM groups), and the loading of BMP-2 (compared to that in the CTL, PM and PMZ groups). The scaffold surface hydrophilicity has been proven to regulate the osteoblast proliferation and spreading in vitro,[47] and degradation of MBGs could release silicon and calcium ions that play an important role in cell proliferation.[48] In addition, ZIF-8 can effectively promote osteoblast proliferation and spreading.[49]

Osteoblasts secrete extracellular matrix proteins such as ALP, COL1, OPN and OCN, and the deposition of calcium and COL1 provides structural support to the skeleton.[50] In this study, it was found that the PMZB scaffold could significantly promote the osteogenic differentiation of cells on the material surface, enhance ALP expression and calcium nodule formation, and increase the expression of osteogenic differentiation-related genes (ALP, COL1, OPN and OCN). On the one hand, slowly released BMP-2 promoted osteogenic differentiation.[51] On the other hand, the degradation of ZIF-8 and the released Zn were beneficial for osteogenesis.[49,52] A previous study showed that nanoscale ZIF-8 coating on titanium could effectively promote osteoblast differentiation, and increase the expression of osteogenic-related genes such as ALP, Runt-related transcription factor-2 (Runx2), OCN and BMP 2, and the ZIF-8 coating could slowly degrade approximately 19.1% of $Zn^{2+}$ within 24 h in the body fluid environment.[49] Another study has shown that $Zn^{2+}$ can enhance the ALP activity of osteoblasts and affect the synthesis of OPN and OCN, leading to changes in the expression level of Runx2 and other osteogenesis-related genes.[52] In addition, the degradation of MBG in PMZB scaffold released Ca, Si, and P ions, which also promoted the osteogenic differentiation of M3T3-E1 cells.[53]

The most intuitive method for evaluating the bone repair ability of materials is to measure the effect of the materials implanted into bone defects in vivo. The calvarial bone defect model is popular among researchers, as the bone structure

allows for the generation of a standardized defect that can be analyzed.[54] A rat calvarial bone defect model was applied to evaluate the bone repair ability of the prepared PMZB scaffold, and it was found using histology and radiographic analysis that the PMZB scaffold could significantly promote new bone formation and bone repair in vivo. As tissue regeneration and repair often take a long time, the controlled release of growth factors is crucial for bone repair and new bone formation.[5] In this study, sustained BMP-2 release was observed over a long time, which was beneficial for osteoblast proliferation and osteogenic differentiation, and could further promote new bone formation. In addition, the silicon ions released from the MBGs play an important role in homeostasis and bone remodeling processes.[53]

BMP-2 is most sought-after growth factor for nonunion bone healing, but its cost inhibits its use in first-line therapeutic strategies.[55] Loading BMP-2 on the PMZB scaffold could achieve the effect of slow controlled release through a three-stage sustained release mechanism and biological effect for promoting bone repair. When used for bone defect repair, the dosage of BMP-2 could be greatly reduced, the cost could be reduced, and the occurrence of heterotopic ossification could be avoided. The selected carrier materials ZIF-8 and MBG could also play roles in osteoconduction and osteoinduction, finally achieving the purpose of effective bone repair.

The optimal bone substitute should be osteoconductive, osteoinductive, osteogenetic, and cost effective, with suitable mechanical properties.[56] The compressive strength of the PMZB scaffolds was within the range of human cancellous bones. The prepared PLGA/MBG scaffold doped with BNP-2@ZIF-8 nanoparticles was proved to be osteoconductive and osteoinductive, with enhanced osteogenic activity and bone repair ability. We considered that the PLGA/MBG/ZIF-8/BMP-2 porous scaffold was a solid alternative bone substitute to existing therapeutics at the non-weight-bearing sites.

## Conclusion

In this study, a sustained release system of composite scaffolds loaded with growth factors was established to achieve the goal of slow controlled release and effective bone repair. A PLGA/MBG porous scaffold was fabricated and incorporated with ZIF-8 nanoparticles loaded with BMP-2 growth factor by a 3D printing method. The PLGA/MBG/ZIF-8/BMP-2 porous scaffold could continuously and slowly release BMP-2, promote the adhesion, proliferation, spreading and osteogenic differentiation of MC3T3-E1 cells in vitro, and enhance new bone formation and bone repair at bone defects in vivo. With enhanced osteogenic activity and bone repair ability, this porous scaffold can be used as a bone graft material to repair bone defects at the non-weight-bearing sites.

## Acknowledgment

## Disclosure

The authors report no conflicts of interest in this work.

## References

1. Agarwal R, Garcia AJ. Biomaterial strategies for engineering implants for enhanced osseointegration and bone repair. *Adv Drug Deliv Rev*. 2015;94:53–62. doi:10.1016/j.addr.2015.03.013
2. Roseti L, Parisi V, Petretta M, et al. Scaffolds for bone tissue engineering: state of the art and new perspectives. *Mater Sci Eng C Mater Biol Appl*. 2017;78:1246–1262. doi:10.1016/j.msec.2017.05.017
3. Kim HD, Amirthalingam S, Kim SL, et al. biomimetic materials and fabrication approaches for bone tissue engineering. *Adv Healthc Mater*. 2017;6 (23). doi:10.1002/adhm.201700612
4. Babilotte J, Guduric V, Le Nihouannen D, et al. 3D printed polymer-mineral composite biomaterials for bone tissue engineering: fabrication and characterization. *J Biomed Mater Res B Appl Biomater*. 2019;107(8):2579–2595. doi:10.1002/jbm.b.34348
5. Qin X, Wu Y, Liu S, et al. Surface modification of polycaprolactone scaffold with improved biocompatibility and controlled growth factor release for enhanced stem cell differentiation. *Front Bioeng Biotechnol*. 2021;9:802311. doi:10.3389/fbioe.2021.802311
6. Gentile P, Chiono V, Carmagnola I, et al. An overview of poly(lactic-co-glycolic) acid (PLGA)-based biomaterials for bone tissue engineering. *Int J Mol Sci*. 2014;15(3):3640–3659. doi:10.3390/ijms15033640
7. Zhu T, Jiang M, Zhang M, et al. Biofunctionalized composite scaffold to potentiate osteoconduction, angiogenesis, and favorable metabolic microenvironment for osteonecrosis therapy. *Bioact Mater*. 2022;9:446–460. doi:10.1016/j.bioactmat.2021.08.005
8. Skidmore S, Hadar J, Garner J, et al. Complex sameness: separation of mixed poly(lactide-co-glycolide)s based on the lactide: glycolide ratio. *J Control Release*. 2019;300:174–184. doi:10.1016/j.jconrel.2019.03.002

9. Wu C, Ramaswamy Y, Zhu Y, et al. The effect of mesoporous bioactive glass on the physiochemical, biological and drug-release properties of poly (DL-lactide-co-glycolide) films. *Biomaterials*. 2009;30(12):2199–2208. doi:10.1016/j.biomaterials.2009.01.029

10. Jang TS, Park SJ, Lee JE, et al. Topography-supported nanoarchitectonics of hybrid scaffold for systematically modulated bone regeneration and remodeling. *Adv Funct Mater*. 2022;32:51.

11. Jang TS, Jung HD, Pan HM, et al. 3D printing of hydrogel composite systems: recent advances in technology for tissue engineering. *Int J Bioprint*. 2018;4(1):126. doi:10.18063/ijb.v4i1.126

12. Schumacher M, Habibovic P, van Rijt S. Mesoporous bioactive glass composition effects on degradation and bioactivity. *Bioact Mater*. 2021;6 (7):1921–1931. doi:10.1016/j.bioactmat.2020.12.007

13. Baino F, Fiorilli S, Vitale-Brovarone C. Composite biomaterials based on sol-gel mesoporous silicate glasses: a review. *Bioengineering*. 2017;4(1). doi:10.3390/bioengineering4010015

14. Kim N, Lee H, Han G, et al. 3D-printed functional hydrogel by DNA-induced biomineralization for accelerated diabetic wound healing. *Adv Sci*. 2023;10(17):e2300816. doi:10.1002/advs.202300816

15. Alksne M, Kalvaityte M, Simoliunas E, et al. In vitro comparison of 3D printed polylactic acid/hydroxyapatite and polylactic acid/bioglass composite scaffolds: insights into materials for bone regeneration. *J Mech Behav Biomed Mater*. 2020;104:103641. doi:10.1016/j.jmbbm.2020.103641

16. Wu C, Fan W, Chang J, et al. Mesoporous bioactive glass scaffolds for efficient delivery of vascular endothelial growth factor. *J Biomater Appl*. 2013;28(3):367–374. doi:10.1177/0885328212453635

17. Li X, Wang X, Zhang L, et al. MBG/PLGA composite microspheres with prolonged drug release. *J Biomed Mater Res B Appl Biomater*. 2009;89 (1):148–154. doi:10.1002/jbm.b.31197

18. Shi M, Zhai D, Zhao L, et al. Nanosized mesoporous bioactive glass/Poly(lactic-co-glycolic Acid) composite-coated CaSiO 3 scaffolds with multifunctional properties for bone tissue engineering. *Biomed Res Int*. 2014;2014:323046. doi:10.1155/2014/323046

19. Li J, Wang C, Gao G, et al. MBG/ PGA-PCL composite scaffolds provide highly tunable degradation and osteogenic features. *Bioact Mater*. 2022;15:53–67. doi:10.1016/j.bioactmat.2021.11.034

20. Gomez-Cerezo N, Casarrubios L, Saiz-Pardo M, et al. Mesoporous bioactive glass/varepsilon-polycaprolactone scaffolds promote bone regeneration in osteoporotic sheep. *Acta Biomater*. 2019;90:393–402. doi:10.1016/j.actbio.2019.04.019

21. Chen S, Jian Z, Huang L, et al. Mesoporous bioactive glass surface modified poly(lactic-co-glycolic acid) electrospun fibrous scaffold for bone regeneration. *Int J Nanomedicine*. 2015;10:3815–3827. doi:10.2147/IJN.S82543

22. Cheng T, Qu H, Zhang G, et al. Osteogenic and antibacterial properties of vancomycin-laden mesoporous bioglass/PLGA composite scaffolds for bone regeneration in infected bone defects. *Artif Cells Nanomed Biotechnol*. 2018;46(8):1935–1947. doi:10.1080/21691401.2017.1396997

23. Li L, Lu H, Zhao Y, et al. Functionalized cell-free scaffolds for bone defect repair inspired by self-healing of bone fractures: a review and new perspectives. *Mater Sci Eng C Mater Biol Appl*. 2019;98:1241–1251. doi:10.1016/j.msec.2019.01.075

24. Lee H, Lee M-K, Cheon K-H, et al. Functionally assembled metal platform as lego-like module system for enhanced mechanical tunability and biomolecules delivery. *Mater Des*. 2021;207:109840. doi:10.1016/j.matdes.2021.109840

25. Halloran D, Durbano HW, Nohe A. Bone morphogenetic protein-2 in development and bone homeostasis. *J Dev Biol*. 2020;8(3):19. doi:10.3390/jdb8030019

26. Lee H, Lee M-K, Han G, et al. Customizable design of multiple-biomolecule delivery platform for enhanced osteogenic responses via 'tailored assembly system. *Bio-Des Manuf*. 2022;5(3):451–464. doi:10.1007/s42242-022-00190-7

27. Wang Q, Sun Y, Li S, et al. Synthesis and modification of ZIF-8 and its application in drug delivery and tumor therapy. *RSC Adv*. 2020;10 (62):37600–37620. doi:10.1039/D0RA07950B

28. Karakecili A, Topuz B, Korpayev S, et al. Metal-organic frameworks for on-demand pH controlled delivery of vancomycin from chitosan scaffolds. *Mater Sci Eng C Mater Biol Appl*. 2019;105:110098. doi:10.1016/j.msec.2019.110098

29. Hoseinpour V, Shariatinia Z. Applications of zeolitic imidazolate framework-8 (ZIF-8) in bone tissue engineering: a review. *Tissue Cell*. 2021;72:101588. doi:10.1016/j.tice.2021.101588

30. Maleki A, Shahbazi MA, Alinezhad V, et al. The progress and prospect of zeolitic imidazolate frameworks in cancer therapy, antibacterial activity, and biomineralization. *Adv Healthc Mater*. 2020;9(12):e2000248. doi:10.1002/adhm.202000248

31. Anand A, Kundu B, Balla VK, et al. Synthesis and physico-chemical characterization of different mesoporous bioactive glass nanopowders: in-vitro SBF activity and cytotoxicity. *Trans Indian Ceram Soc*. 2018;77(2):106–117. doi:10.1080/0371750X.2018.1465357

32. Li Y, Zhu J, Zhang X, et al. Drug-delivery nanoplatform with synergistic regulation of angiogenesis-osteogenesis coupling for promoting vascularized bone regeneration. *ACS Appl Mater Interfaces*. 2023;15(14):17543–17561. doi:10.1021/acsami.2c23107

33. Toprak O, Topuz B, Monsef YA, et al. BMP-6 carrying metal organic framework-embedded in bioresorbable electrospun fibers for enhanced bone regeneration. *Mater Sci Eng C Mater Biol Appl*. 2021;120:111738. doi:10.1016/j.msec.2020.111738

34. Ma R, Tang S, Tan H, et al. Preparation, characterization, in vitro bioactivity, and cellular responses to a polyetheretherketone bioactive composite containing nanocalcium silicate for bone repair. *ACS Appl Mater Interfaces*. 2014;6(15):12214–12225. doi:10.1021/am504409q

35. Ma R, Yu Z, Tang S, et al. Osseointegration of nanohydroxyapatite- or nano-calcium silicate-incorporated polyetheretherketone bioactive composites in vivo. *Int J Nanomedicine*. 2016;11:6023–6033. doi:10.2147/IJN.S115286

36. Wu C, Ramaswamy Y, Zreiqat H. Porous diopside (CaMgSi(2)O(6)) scaffold: a promising bioactive material for bone tissue engineering. *Acta Biomater*. 2010;6(6):2237–2245. doi:10.1016/j.actbio.2009.12.022

37. Ahmadian E, Eftekhari A, Janas D, et al. Nanofiber scaffolds based on extracellular matrix for articular cartilage engineering: a perspective. *Nanotheranostics*. 2023;7(1):61–69. doi:10.7150/ntno.78611

38. Ramazanli VN. Effect of pH and temperature on the synthesis of silver nano particles extracted from olive leaf. *Adv Environ Biol*. 2021;6 (2):169–173.

39. Ahmadov IS, Bandaliyeva AA, Nasibova AN, et al. The synthesis of the silver nanodrugs in the medicinal plant baikal skullcap (Scutellaria baicalensis Georgi) and their antioxidant, antibacterial activity. *Adv Environ Biol*. 2020;5(2):103–118.

40. Atienza-Roca P, Cui X, Hooper GJ, et al. Growth factor delivery systems for tissue engineering and regenerative medicine. *Adv Exp Med Biol*. 2018;1078:245–269.

41. Shen X, Zhang Y, Gu Y, et al. Sequential and sustained release of SDF-1 and BMP-2 from silk fibroin-nanohydroxyapatite scaffold for the enhancement of bone regeneration. *Biomaterials*. 2016;106:205–216. doi:10.1016/j.biomaterials.2016.08.023

42. Suliman S, Xing Z, Wu X, et al. Release and bioactivity of bone morphogenetic protein-2 are affected by scaffold binding techniques in vitro and in vivo. *J Control Release*. 2015;197:148–157. doi:10.1016/j.jconrel.2014.11.003

43. Gao L, Chen Q, Gong T, et al. Recent advancement of imidazolate framework (ZIF-8) based nanoformulations for synergistic tumor therapy. *Nanoscale*. 2019;11(44):21030–21045. doi:10.1039/C9NR06558J

44. Zou F, Jiang J, Lv F, et al. Preparation of antibacterial and osteoconductive 3D-printed PLGA/Cu(I)@ZIF-8 nanocomposite scaffolds for infected bone repair. *J Nanobiotechnology*. 2020;18(1):39. doi:10.1186/s12951-020-00594-6

45. Felgueiras HP, Evans MDM, Migonney V. Contribution of fibronectin and vitronectin to the adhesion and morphology of MC3T3-E1 osteoblastic cells to poly(NaSS) grafted Ti6Al4V. *Acta Biomater*. 2015;28:225–233. doi:10.1016/j.actbio.2015.09.030

46. Geng Z, Ji L, Li Z, et al. Nano-needle strontium-substituted apatite coating enhances osteoporotic osseointegration through promoting osteogenesis and inhibiting osteoclastogenesis. *Bioact Mater*. 2021;6(4):905–915. doi:10.1016/j.bioactmat.2020.09.024

47. He J, Chen G, Liu M, et al. Scaffold strategies for modulating immune microenvironment during bone regeneration. *Mater Sci Eng C Mater Biol Appl*. 2020;108:110411. doi:10.1016/j.msec.2019.110411

48. Zhang Y, Xia L, Zhai D, et al. Mesoporous bioactive glass nanolayer-functionalized 3D-printed scaffolds for accelerating osteogenesis and angiogenesis. *Nanoscale*. 2015;7(45):19207–19221. doi:10.1039/C5NR05421D

49. Chen J, Zhang X, Huang C, et al. Osteogenic activity and antibacterial effect of porous titanium modified with metal-organic framework films. *J Biomed Mater Res A*. 2017;105(3):834–846. doi:10.1002/jbm.a.35960

50. Salhotra A, Shah HN, Levi B, et al. Mechanisms of bone development and repair. *Nat Rev Mol Cell Biol*. 2020;21(11):696–711. doi:10.1038/s41580-020-00279-w

51. Liu Y, Yao Q, Sun H. Prostaglandin E2 modulates bone morphogenetic protein-2 induced osteogenic differentiation on a biomimetic 3D nanofibrous scaffold. *J Biomed Nanotechnol*. 2018;14(4):747–755. doi:10.1166/jbn.2018.2490

52. Gao X, Xue Y, Zhu Z, et al. Nanoscale zeolitic imidazolate framework-8 activator of canonical MAPK signaling for bone repair. *ACS Appl Mater Interfaces*. 2021;13(1):97–111. doi:10.1021/acsami.0c15945

53. Vallet-Regi M, Salinas AJ. Mesoporous bioactive glasses for regenerative medicine. *Mater Today Bio*. 2021;11:100121. doi:10.1016/j.mtbio.2021.100121

54. McGovern JA, Griffin M, Hutmacher DW. Animal models for bone tissue engineering and modelling disease. *Dis Model Mech*. 2018;11(4). doi:10.1242/dmm.033084

55. Agrawal V, Sinha M. A review on carrier systems for bone morphogenetic protein-2. *J Biomed Mater Res B Appl Biomater*. 2017;105(4):904–925. doi:10.1002/jbm.b.33599

56. Calori GM, Mazza E, Colombo M, et al. The use of bone-graft substitutes in large bone defects: any specific needs? *Injury*. 2011;42(2):S56–63. doi:10.1016/j.injury.2011.06.011